ACS APPLIED ENERGY MATERIALS

www.acsaem.org Article

Hematite Nanorods Photoanodes Decorated by Cobalt Hexacyanoferrate: The Role of Mixed Oxidized States on the Enhancement of Photoelectrochemical Performance

Saulo Amaral Carminati, Bruno Leuzinger da Silva, José Luiz Bott-Neto, Mauricio Alves de Melo, Jr., Miguel Tayar Galante, Pablo Sebástian Fernández, Claudia Longo, Juliano Alves Bonacin,* and Ana Flávia Nogueira*

Cite This: *ACS Appl. Energy Mater.* 2020, 3, 10097−10107 Read Online

ACCESS | Metrics & More | Article Recommendations | Supporting Information

ABSTRACT: In this work, we report on the incorporation of cobalt hexacyanoferrate (Co-NC-Fe) with different iron oxidation states (Fe^{II} and Fe^{III}) on hematite (α-Fe_2O_3) nanorod photoanodes with a systematic investigation of enhanced photoelectrochemical performance under a neutral pH. A detailed investigation using *in situ* techniques was carried out to understand the fundamental aspects of chemical reactions during photoelectrochemical characterization. The α-Fe_2O_3/Co-NC-Fe photoanodes showed a higher photoelectrochemical performance compared to the individual materials. Despite the higher achieved performance of α-Fe_2O_3/Co-NC-Fe, the elucidation of the main contribution upon Co-NC-Fe incorporation was found to be dependent on the different charge transfer mechanism under light illumination. Therefore, given the complexity of the redox processes that take place in Co-NC-Fe under an applied bias, we have systematically investigated the dark- and light-induced effects on α-Fe_2O_3/Co-NC-Fe by *in situ* UV−vis and Fourier transform infrared spectroscopies. These techniques allowed us to monitor the effect of the electro and photoelectrochemical potential in several redox processes. The insightful results indicate that, in addition to surface state modification effects, the improvement of the photocurrent density may also result from long-lived holes at the electrode surface as a consequence of the electron transfer from the conduction band α-Fe_2O_3 to Co-NC-Fe with a Fe^{III} oxidation state. This indicates a second electron pathway during charge separation, thereby contributing to the increase in the electron−hole pair lifetime and the accumulation of photogenerated holes at the α-Fe_2O_3/Co-NC-Fe photoanode surface to drive water oxidation.

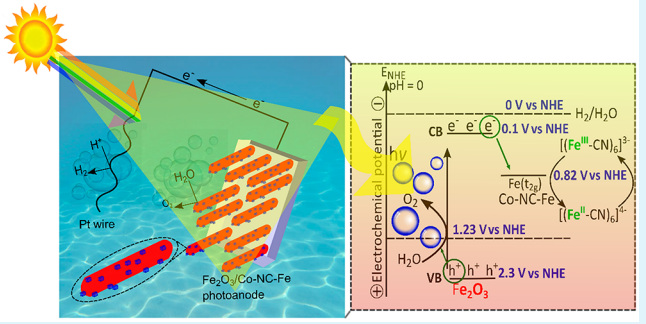

KEYWORDS: *hematite, cobalt hexacyanoferrate, water oxidation, in situ infrared spectroscopy, transient absorption spectroscopy*

1. INTRODUCTION

Extensive work on finding a prospective material that fulfills the several criteria for efficient solar-driven water splitting has still been a long-standing challenge. Therefore, there has been growing interest in the development of semiconductors with a higher stability and performance for water splitting.[1,2] Moreover, developing low-cost photoanodes for photoelectrochemical cells (PEC) that can operate under neutral conditions with a high catalytic performance is of great importance and is a challenge for eco-friendly practical applications.[3]

Hematite (α-Fe_2O_3) is arguably one of the most promising and desirable material to be used as a photoanode in PEC cells for water splitting.[4,5] α-Fe_2O_3 is an *n*-type semiconductor with abundant properties for water oxidation, including high visible light absorption (up to 590 nm), earth-abundant elements, long-term chemical stability, and nontoxicity. Additionally, its bandgap of 2.1 eV provides a high theoretical photocurrent density of 12.6 mA cm^{-2} at air mass (AM) 1.5 G.[6−9] On the other hand, its short hole diffusion length of ∼4 nm, sluggish water oxidation kinetics, and high charge carrier recombination rate are drawbacks that still hamper the use of Fe_2O_3 in PEC applications. Many efforts have been devoted toward minimizing the impact of these shortcomings by improving its performance as a photoanode.[10] Strategies such as functionalization,[11,12] doping,[13−15] heterojunction,[16,17] and surface passivation[18−20] have shown promising results for improved PEC water splitting.

Received: July 28, 2020
Accepted: September 14, 2020
Published: September 14, 2020

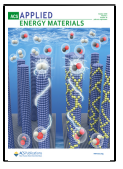

https://dx.doi.org/10.1021/acsaem.0c01782
ACS Appl. Energy Mater. 2020, 3, 10097−10107

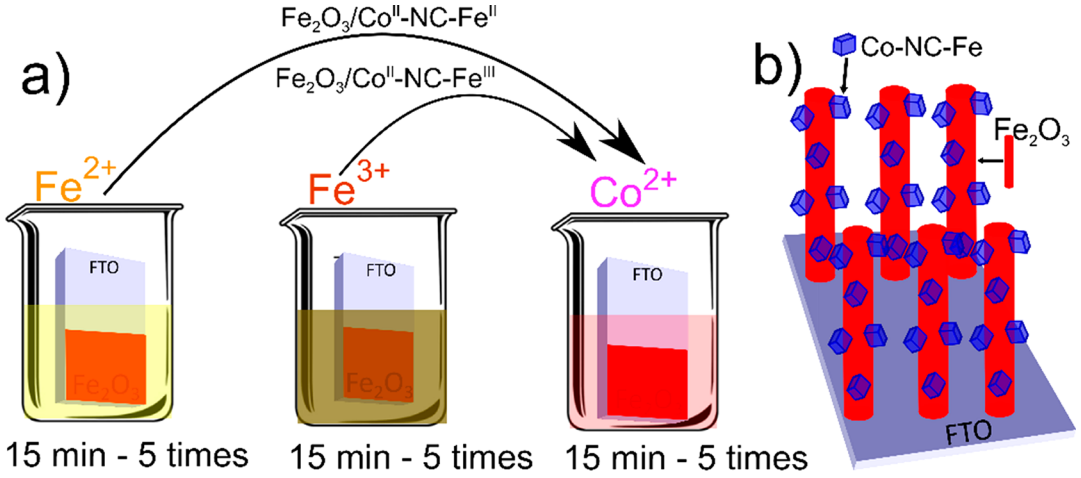

Figure 1. (a) Layer by layer method to synthesize α-Fe_2O_3/Co-NC-Fe photoanodes with Fe atoms in their II and III oxidation states; (b) Illustration of the α-Fe_2O_3 nanorods modified with Co-NC-Fe nanocubes covering their surface.

Prussian blue (PB)-type materials have emerged as potential candidates as electrocatalysts for water oxidation, which can be expressed as $A_xFe[Fe(CN)_6]_y{\cdot}mH_2O$, where A is an alkaline metal, $0 < x < 2$, and $y < 1$.[21] Cobalt hexacyanoferrate (Co-NC-Fe), which has an analogous structure to PB, has shown good electrocatalytic activity, owing to its both fundamental and practical perspectives.[22,23] Such peculiar properties as electrochromism and sensing are based on electron transfer between Fe^{III} and Co^{II} ions in its structure.[24−27] Its application in the oxygen evolution reaction (OER) has been already studied in both basic[28] and neutral[29] media, and more recently, the material has shown improved performance also in acidic conditions.[30] Hegner and co-workers[31] determined by density functional theory (DFT) calculations that there is no allowed hole transfer in α-Fe_2O_3/Co-NC-Fe, due to the misalignment of their energy levels, making charge transfer unfavorable. However, after its incorporation onto a α-Fe_2O_3 photoanode, its photocurrent density was improved, which was assigned to be a consequence of the hole-scavenging character of the interface and the suggestion of different hole-transfer pathways, including tunneling or hopping processes.

In our previous work,[32] we reported the formation of α-Fe_2O_3 nanorods perpendicularly oriented to the fluorine-doped tin oxide (FTO) substrate, which improved the electron transfer along the [110] direction. However, its performance as a photoanode is still far from its theoretical predictability. In the present study, we investigated the modification of its surface with Co-NC-Fe by the combination of different techniques, including *in situ* and/or *operando* measurements. *In situ* and/or *operando* techniques provide conditions to analyze charge dynamics, reaction intermediates, electrode surfaces, and interfaces, which can contribute to the design of more efficient electrocatalysts for PEC water splitting.[33−38] One example is the use of *in situ* Fourier transform infrared (FTIR) spectroscopy, which makes it possible to investigate the fundamental aspects of interfacial processes, allowing progress in the planning of the synthesis of prospective photocatalysts for water splitting.[39−41]

Despite the better PEC performance of α-Fe_2O_3 photoanodes upon Co-NC-Fe incorporation being observed already,[30,31] the major cause of this improvement is still an open question. Therefore, we investigated the effect of different oxidation states of Fe and Co species in Co-NC-Fe analogue structures on their PEC properties. *In situ* techniques (UV−vis and FTIR) coupled with transient absorption spectroscopy (TAS) suggest that the availability of the Fe^{II}/Fe^{III} oxidation process plays a major role in decreasing electron/hole pairs recombination to drive water oxidation. Herein, this work aimed to unveil the mechanisms of synergistic effects by coupling a state-of-the-art α-Fe_2O_3 photoanode with two different Co-NC-Fe materials, based on their starting oxidation states.

2. EXPERIMENTAL SECTION

All chemicals were of analytical grade and used without any further purification. Chemicals: $FeCl_3.6H_2O$ (Sigma-Aldrich, > 98%), Urea (Sigma-Aldrich), $K_3Fe(CN)_6$ (Sigma-Aldrich), $K_4Fe(CN)_6.3H_2O$ (Sigma-Aldrich), $CoCl_2.6H_2O$ (Carlo Erba) Fluorine-doped tin oxide conductive glass (10 Ω /sq, Solaronix, Switzerland).

2.1. Synthesis of α-Fe_2O_3 Nanorods and α-Fe_2O_3/Co-NC-Fe Films. Prior to α-Fe_2O_3 deposition, FTO substrates were thoroughly cleaned using acetone, methanol, and isopropanol. The synthesis of α-Fe_2O_3 nanorods films was carried out by a hydrothermal method, as described in our previous work.[32] The synthesis of Co-NC-Fe materials began with precursor salts containing Fe atoms in the oxidation states of II ($K_4Fe(CN)_6{\cdot}3H_2O$) and III ($K_3Fe(CN)_6$) to form Co^{II}-NC-Fe^{II} and Co^{II}-NC-Fe^{III} respectively. The Co-NC-Fe particles were added on α-Fe_2O_3 photoanodes (α-Fe_2O_3/Co^{II}-NC-Fe^{II} and α-Fe_2O_3/Co^{II}-NC-Fe^{III}). The deposition of Co-NC-Fe on α-Fe_2O_3 films (previously treated at 750 °C) was carried out by the dip-coating method, in which to prepare α-Fe_2O_3/Co^{II}-NC-Fe^{II} and α-Fe_2O_3/Co^{II}-NC-Fe^{III} samples, α-Fe_2O_3 films were immersed first in 0.2 M potassium ferricyanide ($K_3Fe(CN)_6$ corresponding to Fe(III) and $K_4Fe(CN)_6.3H_2O$ corresponding to Fe(II)) and subsequently in 0.04 M $CoCl_2{\cdot}6H_2O$ for 15 min each, as illustrated in Figure 1. The dip-coating sequential method was carried out 5 times with a subsequent drying process at 100 °C between each deposition. After the final coating step, the films were washed and then dried at 80 °C for 2 h. For the sake of comparison, pristine Co-NC-Fe films were also prepared by dip-coating deposition directly onto cleaned FTO substrates.

2.2. Characterization of the Materials. The surface of the as-prepared α-Fe_2O_3 and α-Fe_2O_3/Co-NC-Fe photoanodes was examined by field emission-scanning electron microscopy (Quanta 250 FEG-SEM). An XPS (X-ray photoelectron spectroscopy) analysis was performed using an excitation source of Al Kα ($h\nu$ = 1486.6 eV) radiation and a high-performance hemispheric analyzer (EAC2000) with an ultrahigh vacuum chamber (UHV) that maintained a pressure of 10^{-9} Pa during the measurements. CasaXPS software was

https://dx.doi.org/10.1021/acsaem.0c01782
ACS Appl. Energy Mater. 2020, 3, 10097−10107

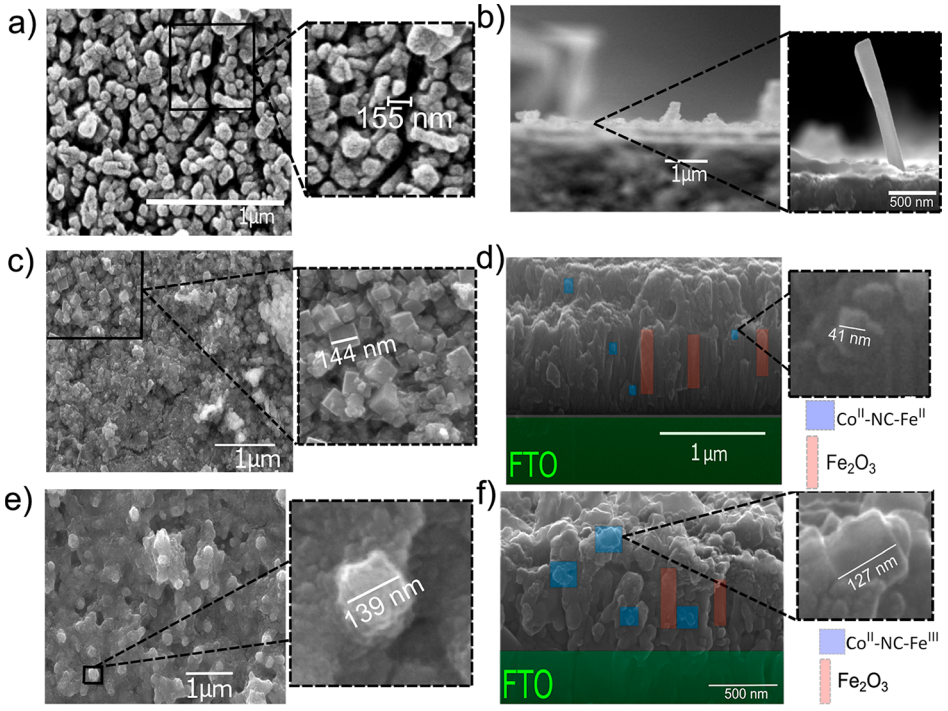

Figure 2. Top-view and cross sectional FEG-SEM images of (a and b) α-Fe_2O_3, (c and d) α-Fe_2O_3/Co^{II}-NC-Fe^{II}, and (e and f) α-Fe_2O_3/Co^{II}-NC-Fe^{III}, respectively. The red and blue marks depict the α-Fe_2O_3 nanorods and Co-NC-Fe nanocubes, respectively.

employed for the data adjustment, setting the C 1s peak at 284.8 eV as the reference for calibration.

2.3. Photoelectrochemical Characterization. All PEC experiments were carried out under ambient conditions using a potentiostat/galvanostat (μAutolab III). The three-electrode cell configuration was composed of α-Fe_2O_3, α-Fe_2O_3/Co^{II}-NC-Fe^{II}, and α-Fe_2O_3/Co^{II}-NC-Fe^{III} photoanodes (1 cm × 1 cm) as the working electrode (WE), Ag/AgCl in saturated KCl (3 mol L^{-1}) as the reference electrode (RE), and a platinum wire as the counter electrode (CE). The electrolyte was a buffer solution of 0.1 M KPi (KH_2PO_4/K_2HPO_4) at pH 7. Linear sweep (LSV) and cyclic voltammetry (CV) measurements were carried out at a scan rate of 10 mV s^{-1} in the range of −0.1 to 1.2 V versus Ag/AgCl. Chronoamperometry experiments were performed using the same PEC cell in 0.1 KPi (pH = 7) under light illumination at 0.62 $V_{Ag/AgCl}$ (1.23 V_{RHE}). The IPCE (incident photon-to-current conversion efficiency) values were obtained according to the following equation:

$$\mathrm{IPCE}(\lambda) = (J^{*}1240/P_{light}{}^{*}\lambda) \quad (1)$$

where J is the measured photocurrent density (mA cm^{-2}) and 1240 is the value obtained by multiplying h (Planck's constant) by c (speed of light). P_{light} is the monochromatic illumination power (mW cm^{-2}), and λ is the wavelength (nm) on the incident light. The measurements were carried out in a 0.1 M KPi aqueous solution (at 0.62 $V_{Ag/AgCl}$) using Metrohm/ThorLabs setup equipment.

2.4. Transient Absorption Spectroscopy (TAS) Measurements. TAS measurements at a microsecond to second time scale were acquired by a pump−probe transient absorption spectrometer (Optical Building Blocks Corporation, OBB) using a three-electrode cell. A nitrogen laser was used as an UV excitation source (337 nm, pulse width = 6 ns, typically 1 Hz repetition, 150 μJ cm^{-2} $pulse^{-1}$). The transmitted probe pulse was achieved using a light source (100 W tungsten lamp), and the wavelength at 650 nm was selected using an OBB monochromator. The measurements were conducted on α-Fe_2O_3 and α-Fe_2O_3/Co-NC-Fe photoanodes in the absence of an external bias and at 0.62 V versus Ag/AgCl (1.23 V_{RHE}), in which the mΔOD is the transient absorption change. The signal amplitude was recorded using a digital oscilloscope (Tektronic, TDS 2022C).

2.5. *In Situ* Characterization: UV−Vis and FTIR Spectroscopy Measurements. *In situ* UV−visible (UV−vis) absorption measurements were collected in the range of 300−800 nm at room temperature through an Agilent Cary 60 UV−vis spectrophotometer and using the same three-electrode PEC cell. All UV−vis measurements were performed in dark conditions under an applied bias from −0.1 to 1.0 V versus Ag/AgCl in 0.1 M KPi (pH 7). *In situ* infrared experiments were conducted on a Shimadzu Prestige-21 spectrometer equipped with a MCT detector. A three-electrode spectroelectrochemical cell with a CaF_2 window attached to the bottom of the cell was used, as described in the literature.[42] More details about our *in situ* FTIR system can be found elsewhere.[43] The α-Fe_2O_3, α-Fe_2O_3/Co^{II}-NC-Fe^{II}, or α-Fe_2O_3/Co^{II}-NC-Fe^{III} materials were deposited onto gold substrates and used as working electrodes (0.785 cm^2). Prior to recording the FTIR spectra, the working electrodes were first activated by 10 cycles at 10 mV s^{-1} and then polarized at −0.1 V versus Ag/AgCl until reaching photocurrent stabilization. Each spectrum was the average of 164 interferograms with 4 cm^{-1} of resolution in the range of 2000−2200 cm^{-1}, the region where CN^- stretching mode frequencies are probed in the presence of Fe and Co as a function of their oxidation states. The measurements under light illumination were performed using a HAS-320 solar simulator (Asahi Spectra) with a compact xenon light source under AM 1.5 G conditions. All spectra are shown as a transmittance percentage, using the spectra taken at −0.1 V as the reference. Thus, positive bands indicate the disappearance and negative bands the generation of species.

3. RESULTS AND DISCUSSION

FEG-SEM images of the α-Fe_2O_3 and α-Fe_2O_3/Co-NC-Fe films revealed that the oriented α-Fe_2O_3 particles exhibit a nanorod shape, whereas Co^{II}-NC-Fe^{II} and Co^{II}-NC-Fe^{III}, successfully deposited over the α-Fe_2O_3 surface, show a cubic aspect. From the top-view FEG-SEM images of the pristine α-Fe_2O_3 (Figure 2a) and the α-Fe_2O_3/Co-NC-Fe films (Figure 2c and e), it can be clearly seen that the Co^{II}-NC-Fe^{II} (∼144 nm) and Co^{II}-NC-Fe^{III} (∼139 nm) nanocubes are not only located at the top of α-Fe_2O_3 nanorods (∼155 nm) but

https://dx.doi.org/10.1021/acsaem.0c01782
ACS Appl. Energy Mater. 2020, 3, 10097−10107

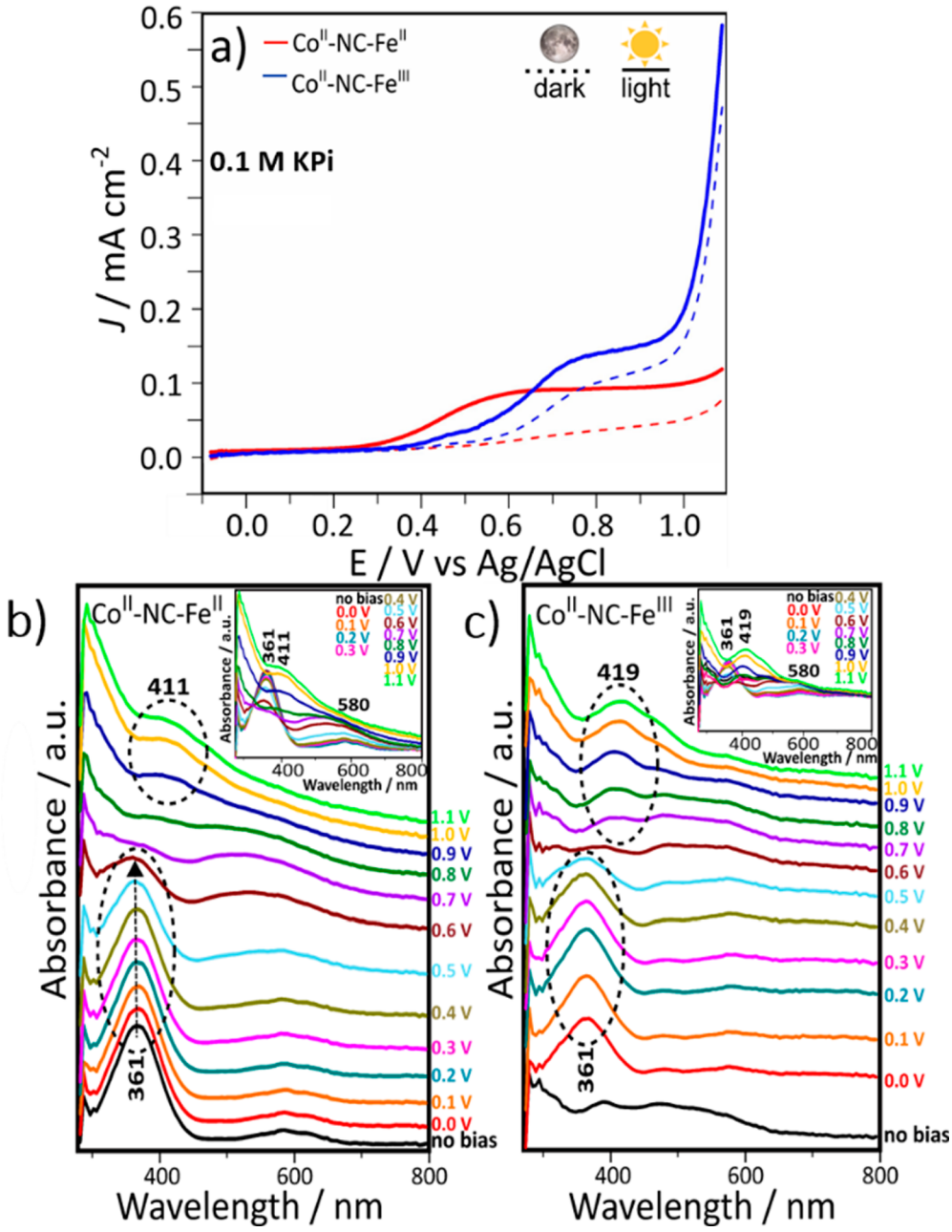

Figure 3. (a) Current−potential profiles of FTO|Co^{II}-NC-Fe^{II} and FTO|Co^{II}-NC-Fe^{III} electrodes in phosphate buffer solution (0.1 M KPi); in situ UV−vis measurements of (b) Co^{II}-NC-Fe^{II} and (c) Co^{II}-NC-Fe^{III} films. The inset shows the as-obtained spectra as a function of the applied bias (vs Ag/AgCl).

also distributed between them. This result was also confirmed by EDX spectra obtained at different regions of the cross-section profile (Figures S1 and S2 in the Supporting Information (SI)).

The chemical composition of the samples was investigated by XPS for the powder materials. The XPS survey spectra (Figure S3) showed the presence of Fe and O for α-Fe_2O_3; for α-Fe_2O_3/Co-NC-Fe samples, Co and N were also identified (Figures S4 and S5). The XPS spectra showed the presence of Fe^{II} in α-Fe_2O_3/Co^{II}-NC-Fe^{II} (from $[Fe(CN)_6]^{4+}$), whereas α-Fe_2O_3/Co^{II}-NC-Fe^{III} mainly consists of Fe^{III} ions, corresponding to $[Fe(CN)_6]^{3+}$ species. The small signal of Fe^{III} in α-Fe_2O_3/Co^{II}-NC-Fe^{II} can be attributed to Fe^{III} ions from α-Fe_2O_3[44] surface linked to $[Fe(CN)_6]^{4+}$. Additionally, a small amount of Co^{III} in both α-Fe_2O_3/Co-NC-Fe samples was observed, where probably Co^{II} is partially oxidized to Co^{III} after mixing with hexacyanoferrate complexes in solution.[31] The formation of Co-NC-Fe performed at ambient conditions can contribute to the oxidation of Co^{II} to Co^{III} (ls, low spin) (see in Reaction S1 in the SI). For a more detailed discussion, see the SI.

First, it should be pointed out that Co^{II}-NC-Fe^{II} and Co^{II}-NC-Fe^{III} present bluish and reddish aspects, respectively. The characterization of Co-NC-Fe films deposited on FTO included electrochemical and *in situ* UV−vis measurements in a phosphate buffer aqueous solution (0.1 M KPi, pH 7.0). The current−potential profiles obtained by linear sweep voltammetry revealed remarkable differences for both electrodes (Figure 3a). In the dark, while the FTO|Co^{II}-NC-Fe^{II} sample exhibited only a slight increase in the current density

https://dx.doi.org/10.1021/acsaem.0c01782
ACS Appl. Energy Mater. 2020, 3, 10097−10107

for an applied potential $E > 0.7$ V (vs Ag/AgCl), the FTO| Co^{II}-NC-Fe^{III} sample presented ca. 0.08 mA cm^{-2} for 0.6 V < E < 0.9 V and a remarkable anodic current for $E > 1.0$ V, probably associated with the oxygen evolution reaction (OER). Under irradiation, both electrodes exhibited an anodic photocurrent. The cyclic voltammograms indicate two redox processes (Figure S6a and b), with cathodic peaks observed at 0.85 and 0.4 V, which can be attributed to Fe^{II}/Fe^{III} and Co^{II}/Co^{III} redox species, respectively.[45] These features were intensified by irradiation, as well as by potential cycling, especially for Co^{II}-NC-Fe^{III} electrodes. *In situ* UV−vis absorption spectra of the Co^{II}-NC-Fe^{II} and Co^{II}-NC-Fe^{III} films (Figure 3b and c) indicate different absorption profiles with an increasing applied potential. For the Co^{II}-NC-Fe^{II} film, the maximum signal at 361 nm, assigned to ligand-to-metal charge transfer (LMCT) of the Co^{II}-NC-Fe^{II} units,[46] is completely quenched at 0.7 V, indicating the complete oxidation of reduced species. For the Co^{II}-NC-Fe^{III} film, there is a broad charge-transfer band between 500 and 600 nm for a spectrum taken for unbiased electrodes, ascribed to the presence of mix-valence Co-NC-Fe species, $K_{0.4}Co_{1.3}[Fe(CN)_6]$ or $KCo[Fe(CN)_6]$.[47] The slight growth of 411, 419 (MLCT, metal-to-ligand charge transfer[24]), and 580 nm (d → d electronic transition in cobalt)[48] signals with a concomitant decrease of a 361 nm signal as the applied potential increases may be ascribed to the formation of oxidized species and consumption of reduced species, respectively. Additionally, the increase in the band signal at 420 nm may be associated with free $Fe(CN)_6$ species and to switching between reduced Co^{II}-Fe^{II} to oxidized Co^{III}-Fe^{II}/Co^{II}-Fe^{III} states.[49] Interestingly, we noticed that MLCT occurs at a lower potential in Co^{II}-NC-Fe^{III} (Figure 3c, 0.7 V) than in Co^{II}-NC-Fe^{II} (Figure 3b, 0.9 V). Moreover, the starting electronic state of Co^{II}-NC-Fe^{III} is achieved at 0.7 V, indicating a high stability over the applied potential. The broadband at the region around 550 nm is assigned to the charge-transfer (CT) from Fe^{II} to Co^{III}.[50,51]

PEC measurements of bare α-Fe_2O_3, α-Fe_2O_3/Co^{II}-NC-Fe^{II}, and α-Fe_2O_3/Co^{II}-NC-Fe^{III} electrodes are shown in Figure 4. It is important to point out that α-Fe_2O_3 photoanodes show better PEC performance in a strongly alkaline electrolyte.[10,52] Mild conditions (neutral pH) were used herein because PB analogues present poor stability under alkaline conditions, in which ligand exchange between the CN^- and OH^- results in their complete dissolution.[53] As expected at this pH, a negligible photocurrent density was exhibited by the pristine α-Fe_2O_3 even at high potentials. Upon Co^{II}-NC-Fe^{II} and Co^{II}-NC-Fe^{III} depositions on the α-Fe_2O_3 electrodes (Figure 4), a remarkable enhancement of the PEC performance is observed, indicating a synergistic effect between α-Fe_2O_3 and Co-NC-Fe.[31,54] Although, α-Fe_2O_3/Co^{II}-NC-Fe^{II} has its photocurrent density stabilized at 0.3 V, reaching a plateau of about 0.25 mA cm^{-2}, α-Fe_2O_3/Co^{II}-NC-Fe^{III} continues to rise considerably, attaining approximately 1.1 mA cm^{-2} at 1.2 $V_{Ag/AgCl}$. Positive transients in the photocurrent under light illumination, associated with the accumulation of holes at the electrode surface[55] were observed, as shown in chopped-light experiment (Figure 4b). Although no decrease in the current transients was observed for α-Fe_2O_3/Co^{II}-NC-Fe^{II} during the whole potential sweep, α-Fe_2O_3/Co^{II}-NC-Fe^{III} presented a considerable drop (smaller spikes) at higher potentials, indicating the enhanced injection of holes from the electrode to the electrolyte, ready to drive water oxidation. The α-Fe_2O_3/Co-NC-Fe photoanodes are stable and they generate high

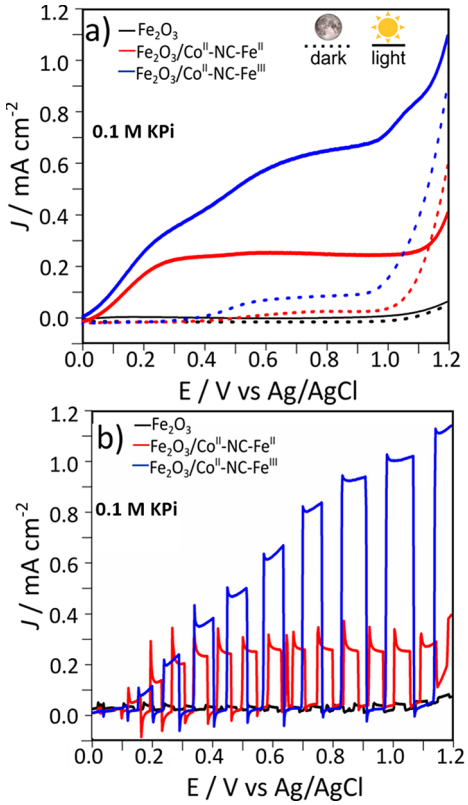

Figure 4. α-Fe_2O_3, α-Fe_2O_3/Co^{II}-NC-Fe^{II}, and α-Fe_2O_3/Co^{II}-NC-Fe^{III} electrodes in 0.1 M KPi: (a) current−potential profile in the dark and under irradiation and (b) under intermittent irradiation. The measurements were carried out at a scan rate of 10 mV s^{-1}.

photocurrents in the range of milliamperes per square centimeter at neutral pH values, which is desirable for eco-friendly and commercial applications on a practical large scale.[56]

The PEC stability of the electrodes was investigated by chronoamperometry by polarization at different potentials. The photocurrent density values were maintained for measurements performed under intermittent irradiation over 15 min, as shown in Figure S7. Also, we observed a decrease in the spike intensity upon increasing the potential. These spikes, which can be associated with the accumulation of holes at the surface, also decreased for α-Fe_2O_3/Co-NC-Fe electrodes, indicating an improvement of charge transport upon Co-NC-Fe incorporation. Additionally, the photocurrent density was measured while the electrodes were polarized at 0.62 V vs Ag/AgCl (or 1.23 V_{RHE}) during more than 10 h (Figure S8a and b). The photocurrent response considerably decreased by almost 75%, resulting in 0.04 mA cm^{-2} for α-Fe_2O_3/Co^{II}-NC-Fe^{II} and 0.14 mA cm^{-2} for α-Fe_2O_3/Co^{II}-NC-Fe^{III}, until reaching a stable state. Surprisingly, after switching the light off and on again, we found the photocurrent density to be almost completely retrieved (Figure S8c and d), indicating the same performance as that obtained for freshly prepared Fe_2O_3/Co-NC-Fe photoanodes (Figure S8), indicating a negligible photocorrosion.

The charge carrier dynamics on α-Fe_2O_3 and α-Fe_2O_3/Co-NC-Fe photoanodes were evaluated by TAS experiments. The transient absorption was probed at 650 nm within a microsecond to second time scale without and with the application of an external electrical bias of 0.62 V versus Ag/

https://dx.doi.org/10.1021/acsaem.0c01782
ACS Appl. Energy Mater. 2020, 3, 10097−10107

AgCl (corresponding to 1.23 V versus RHE), as shown in Figure 5. The fast decay of the hole lifetime on early time

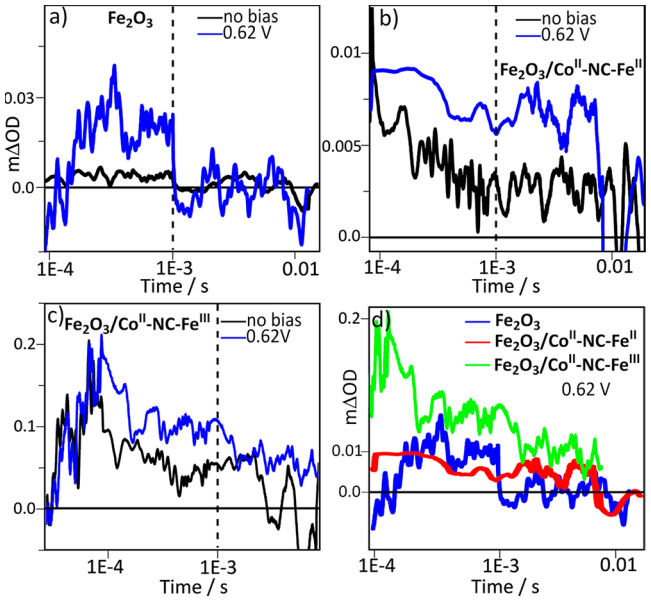

Figure 5. Dynamics of photogenerated holes (probed at 650 nm) in (a) α-Fe_2O_3, (b) α-Fe_2O_3/Co^{II}-NC-Fe^{II}, and (c) α-Fe_2O_3/Co^{II}-NC-Fe^{III} photoanodes; (d) transient absorption decay of the materials at 0.62 V vs Ag/AgCl (1.23 V_{RHE}). The measurements were carried out in the absence or under 0.62 $V_{Ag/AgCl}$ of an applied bias in 0.1 M KPi (pH 7).

scales is well-known in the literature,[57,58] as observed in Figure 5a. The decay kinetics after Co-NC-Fe modification are shown in Figure 5b and c. It is worth mentioning that Co-NC-Fe did not affect the probing of holes at this wavelength. The first observation is the effect of the applied bias on the increased signal amplitude for all electrodes, in which a much longer lifetime of the photogenerated holes is observed upon Co-NC-Fe modification on the α-Fe_2O_3 surface. Moreover, we noticed a slower power-law decay upon Co-NC-Fe modification, which was more pronounced for α-Fe_2O_3/Co^{II}-NC-Fe^{III}, corroborating with the best PEC performance among the samples. The results suggest that ultrafast electron/hole recombination is retarded, leading to the formation of longer-lived holes. Interestingly, taking the signal amplitude at 1 ms as a reference, the signal of photogenerated holes in pristine α-Fe_2O_3 reaches zero, in contrast to that of the modified α-Fe_2O_3 photoanodes, even for unbiased measurements. Additionally, the signal amplitude of photogenerated holes in the α-Fe_2O_3/Co-NC-Fe photoanode is increased by almost 20-fold (Figure 5d) compared to that of the pristine Fe_2O_3 photoanode, followed by a slower decay profile, indicating a more effective charge separation.

IPCE spectra of the electrodes are shown in Figure S9. We observed an appreciable improvement in the IPCE intensity upon α-Fe_2O_3 modification with Co-NC-Fe. Correlating with PEC performances, we observed that despite the Fe_2O_3-Co-NC-Fe^{II} photoanode presenting a lower photocurrent density in $J-V$ curves, its IPCE profile is more intense when compared to the α-Fe_2O_3/Co^{II}-NC-Fe^{III} photoanode. This behavior may be associated with the absorption of the α-Fe_2O_3-Co-NC-Fe^{II} film in the UV region, as observed in Figure 3b. IPCE plots were obtained at a given applied potential (in this case, a constant potential of 0.62 V versus Ag/AgCl), and their values were only obtained after the photocurrent stabilization. The α-Fe_2O_3/Co^{II}-NC-Fe^{II} photoanode was observed to be more stable than α-Fe_2O_3/Co^{II}-NC-Fe^{III} in this experiment.

Up to this point, we have seen a substantial enhancement of the PEC performance of α-Fe_2O_3/Co-NC-Fe in comparison to bare α-Fe_2O_3 photoanodes and an increased lifetime of the photogenerated charge carriers. Nonetheless, the main reason for the boosted photocurrent has not yet been fully elucidated. Likewise, it was perceptible that despite the better PEC performance observed for both α-Fe_2O_3/Co-NC-Fe photoanodes, α-Fe_2O_3/Co^{II}-NC-Fe^{III} was found to have a stronger influence on the photocurrent density generation at higher potentials, whereas α-Fe_2O_3/Co^{II}-NC-Fe^{II} achieved a plateau photocurrent density. In order to understand these observations in terms of potential-induced chemical changes, we performed *in situ* UV−vis (in the dark) and FTIR studies (in the dark and under light illumination).

Although *in situ* UV−vis measurements have shown chemical changes associated with redox processes under an applied potential in the dark, *in situ* FTIR experiments were performed to gain a deeper understanding about possible changes in the oxidation between dark and light conditions. Herein, it is expected that *in situ* FTIR spectroscopy brings additional evidence about the redox processes observed in CV measurements at a scan rate of 10 mV s^{-1} (Figure S6). Co-NC-Fe is potentially attractive for infrared investigations since its structure contains strongly absorbing CN^- functional group.[59] It is important to point out that Co-NC-Fe samples may exist in four different combinations of Co and Fe oxidation states, i.e., Co^{II}/Fe^{II}, Co^{III}/Fe^{II}, Co^{II}/Fe^{III}, and Co^{III}/Fe^{III}, in which the CN^- stretching mode frequencies are seen at different wavenumbers. To the best of our knowledge, this is the first report about *in situ* FTIR measurements on α-Fe_2O_3/Co-NC-Fe, even in the dark and under light illumination.

Prior to *in situ* FTIR experiments, CV measurements of each material on gold substrates were performed (Figure S10a and b) to attain a stationary state. Figure 6a and b show the *in situ* FTIR spectra of α-Fe_2O_3/Co^{II}-NC-Fe^{II} and α-Fe_2O_3/Co^{II}-NC-Fe^{III} obtained in the dark during a positive potential sweep. Afterward, in order to clarify the different aspects of dark- and light-driven electrochemical processes in α-Fe_2O_3/Co^{II}-NC-Fe^{II} and α-Fe_2O_3/Co^{II}-NC-Fe^{III}, the measurements under light illumination (Figure 6c and d) were repeated. The spectra of Co-NC-Fe without α-Fe_2O_3 are shown in Figure S10c and d. Figure 6 shows only the signals coming from the species formed (negative signals) during the increase of the electrochemical potential. The consumed species (seen as positive signals) are shown in the full spectra in Figure S11.

Bands due to the oxidation of Co^{II} and/or Fe^{II} were observed, in accordance with XPS results. The attribution of the bands was based on the literature[49,60] and in spectra obtained with standards $(K_3Fe(CN)_6$ and $K_4Fe(CN)_6.3H_2O$ precursors) in solutions (Figure S12) and a summary of the band assignments can be found in Table S1. Figure 6a and b in the dark show that the presence of α-Fe_2O_3 strongly impacts the results for Co^{II}-NC-Fe^{III}. A band around 2115 cm^{-1} arises at 0.1−0.2 V due to the stretching of the CN-Co^{III}/Fe^{II} configuration, indicating the oxidation of Co^{II} to Co^{III} (CN^- was set in front of the oxidation state of the ions to indicate that we are referring to the stretching mode and not the material).[61] All the bands changed their frequencies with the

https://dx.doi.org/10.1021/acsaem.0c01782
ACS Appl. Energy Mater. 2020, 3, 10097−10107

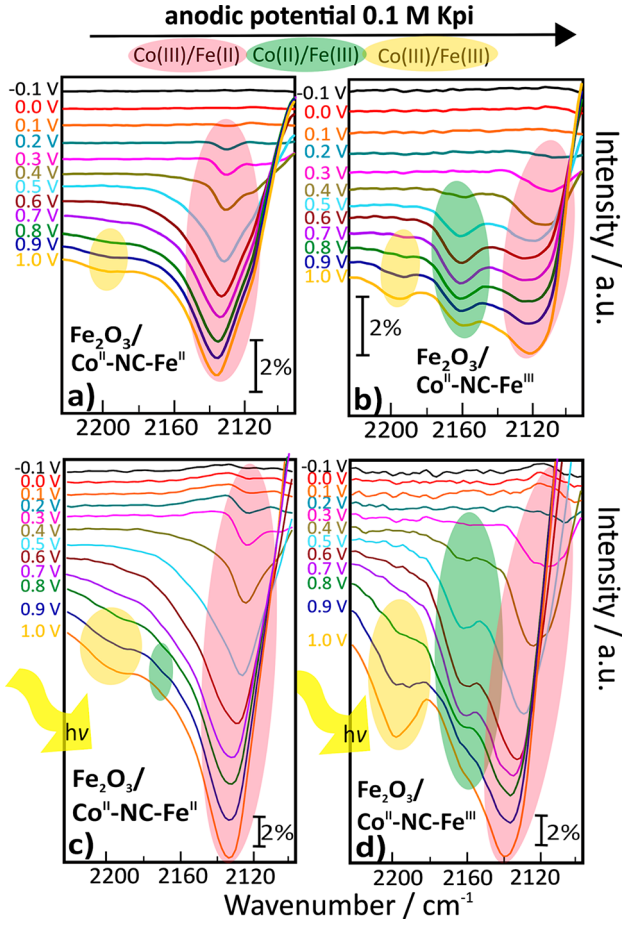

Figure 6. *In situ* FTIR spectra of (a) α-Fe_2O_3/Co^{II}-NC-Fe^{II} and (b) α-Fe_2O_3/Co^{II}-NC-Fe^{III} in the dark and (c) α-Fe_2O_3/Co^{II}-NC-Fe^{II} and (d) α-Fe_2O_3/Co^{II}-NC-Fe^{III} under light illumination. The spectra were recorded from −0.1 to 1.0 V vs Ag/AgCl of an applied bias (1 mV s^{-1}) in 0.1 M KPi (pH 7). The circles depict the appearance of the Co^{III}/Fe^{II} (rose), Co^{II}/Fe^{III} (green), and Co^{III}/Fe^{III} (yellow) oxidized species as a function of the applied bias.

electrochemical potential, which is due to the well-known Stark effect.[62]

Very interestingly, the band at 2160 cm^{-1} is almost exclusive for Co^{II}-NC-Fe^{III} and α-Fe_2O_3/Co^{II}-CN-Fe^{III} and can be assigned to the regeneration of Fe^{III} after the application of a positive bias. The full oxidization of Fe^{II} to Fe^{III} is a process limited by the diffusion of K^+ ions, and its kinetics demands two-K^+ extraction from the framework of the Co-NC-Fe structure for the charge balance of the compounds within the lattice[63] (Reaction S2), which may be assumed as the reason for the absence of the CN-Co^{II}/Fe^{III} signal at 2160 cm^{-1} under an applied bias for Co^{II}-NC-Fe^{II} and α-Fe_2O_3/Co^{II}-CN-Fe^{II}. As observed in Figure 6, Co^{II}-NC-Fe^{III} and α-Fe_2O_3/Co^{II}-CN-Fe^{III} presented reversible intercalation kinetics, since both Co and Fe ions can be reduced/oxidized during the application of an external bias. On the other hand, Co^{II}-NC-Fe^{II} and α-Fe_2O_3/Co^{II}-CN-Fe^{II} did not present this feature; as a consequence, the band at 2160 cm^{-1} was not detected, even at higher potentials.

Finally, a relatively low intensity band emerges at 2190 cm^{-1} due to the formation of either CN-Co^{III}-Fe^{III} or a second type of Co^{II}-NC-Fe^{III} species,[64] which only appears at higher potentials (≥0.8 V) and seems to be more intense for Co^{II}-NC-Fe^{III}. Under light illumination, Figure 6c and d, despite that the bands are the same as in the dark, the Co^{III}-NC-Fe^{II} signal appears at lower potentials and is greatly enhanced (Figure S13), especially for α-Fe_2O_3/Co^{II}-NC-Fe^{III}, which presented a higher intensity band signal at 2125 cm^{-1}, indicating the preferential formation of Fe^{II} species. Meanwhile, the signal of Co^{III}-NC-Fe^{III} for α-Fe_2O_3/Co^{II}-NC-Fe^{III} (Figure 6d) is also increased at higher potentials, indicating that Fe ions have their both 2+ and 3+ oxidation states formed simultaneously under light illumination with the application of an external bias.

Returning to the voltammograms in Figures 3a and 4a and correlating them with the *in situ* FTIR spectra, we assign the dark current to the oxidation of Fe^{II} to Fe^{III} in the Co-NC-Fe catalyst under an applied bias and not to any water oxidation process. *In situ* FTIR spectra show the oxidation of Fe^{II} to Fe^{III}

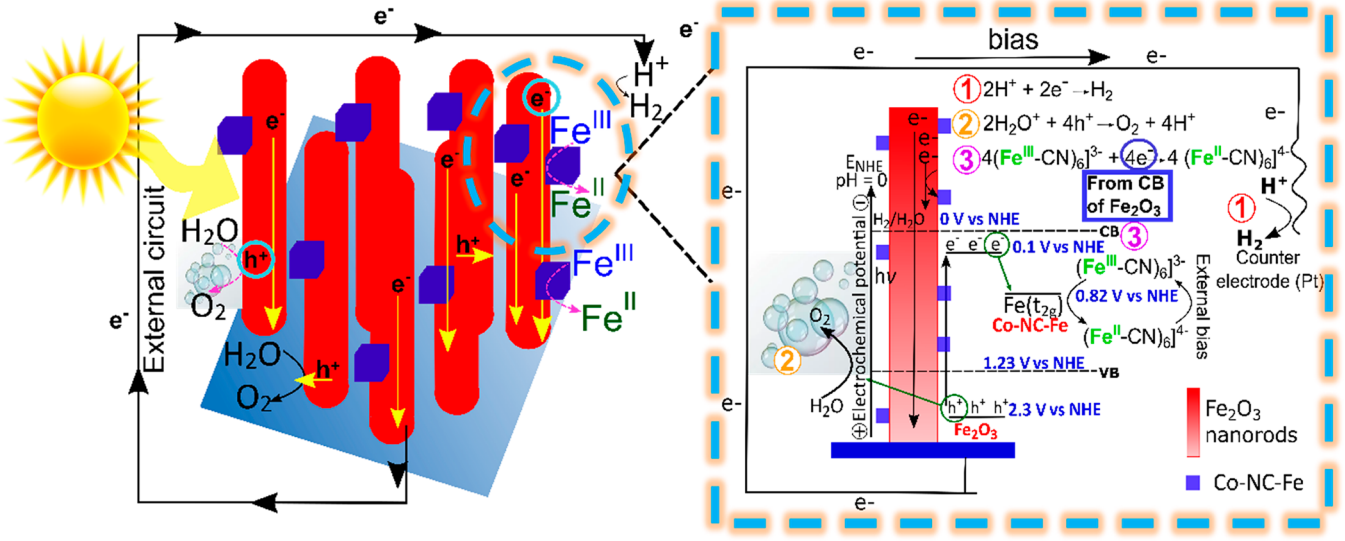

Figure 7. Schematic illustration of charge carrier transport in the α-Fe_2O_3/Co^{II}-NC-Fe^{III} photoanode and an energy diagram depicting the three proposed reactions during PEC characterization, one of which is the photoinduced electron transfer from the CB of α-Fe_2O_3 to $[Fe(CN)_6]^{3-}$ in Co-NC-Fe. The band edge positions are shown at pH 0 relative to NHE.[8,66]

https://dx.doi.org/10.1021/acsaem.0c01782
ACS Appl. Energy Mater. 2020, 3, 10097−10107

starting at ~0.4 V, a region where the dark current starts to increase. *In situ* FTIR allowed us to follow the oxidation of Co and Fe ions induced by the electrochemical potential in Co-NC-Fe and α-Fe_2O_3/Co-NC-Fe. The results in the dark demonstrate that the first oxidation reaction is the Co^{II}/Co^{III} redox species at lower potentials (0.1−0.2 $V_{Ag/AgCl}$), followed by Fe^{II}/Fe^{III} ions (0.4 $V_{Ag/AgCl}$), in which the latter is observed exclusively for Co^{II}-NC-Fe^{III}-based photoanodes. Considering the strong synergistic effect of the light and α-Fe_2O_3/Co^{II}-NC-Fe^{III} photoanode, these experiments clearly suggest that the formation of the Co^{III}/Fe^{II} pair is crucial toward an optimal PEC performance.

In the results obtained by *in situ* FTIR experiments, the most noticeable feature is that the formation of the Co^{II}/Fe^{III} species (at 2160 cm^{-1}) is observed only for Co^{II}-NC-Fe^{III} with and without α-Fe_2O_3. The use of $[Fe(CN)_6]^{3-}/[Fe(CN)_6]^{4-}$ as a redox mediator[65] in Z-scheme applications under neutral conditions has been studied and shows the excellent activity for water oxidation using Fe^{III} as an electron acceptor. Yamamoto and co-workers[66] have shown that upon band gap excitation of titania nanosheets, Prussian blue (Fe^{III}−CN-Fe^{II}) can be photoreduced to Prussian white (Fe^{II}-CN-Fe^{II}) by receiving electrons from titania nanosheets. Figure 7 shows the schematic illustration of the α-Fe_2O_3/Co-NC-Fe phoanode during PEC characterization. As illustrated in the scheme in Figure 7, when the α-Fe_2O_3/Co-NC-Fe photoanode is photoexcited, electron/hole pairs are created. The electrons are transferred along α-Fe_2O_3 nanorods toward the FTO substrate and then to the counter electrode (Pt wire) to drive proton reduction (H^+/H_2) (reaction 1 in Figure 7), whereas holes are accumulated at the photoanode/electrolyte interface to drive water oxidation (H_2O/O_2) (reaction 2 in Figure 7), as expected for an *n*-type semiconductor.

As observed in Figure 7, even if the conduction band (CB) position of α-Fe_2O_3[8,67] is below that of proton reduction, it is still above Fe(t_{2g}) of Co-NC-Fe.[65] We propose a third reaction (reaction 3 in Figure 7) associated with the photoreduction of Co^{II}-NC-Fe^{III} by electron transfer from CB of α-Fe_2O_3 to the $[Fe(CN)_6]^{3-}$ species in Co-NC-Fe. This reaction is proposed in the situation where the photogenerated electrons, while migrating along the nanorod boundary of α-Fe_2O_3, find a Co^{II}-NC-Fe^{III} species before reaching the FTO substrate and then taking part in Fe^{III} reduction. Such a mechanism is supported by *in situ* FTIR experiments, where, under light illumination, the Co^{III}-NC-Fe^{II} species have their signal intensified, indicating the photoreduction of Fe^{III} ions by the electrons in the CB of α-Fe_2O_3 at higher potentials. Correlating these data with TAS measurements, holes at VB of α-Fe_2O_3 have their lifetime prolonged, suppressing electron/hole recombination and consequently enhancing the photocurrent density at high potentials. The collection of these electrons at the boundaries of the nanorods (Figure 7, left) led holes to accumulate at the surface, remaining available to oxidize water. This would not be expected if Co-NC-Fe particles are in contact with α-Fe_2O_3 nanorods only at the electrode surface.

Such observations can also be supported by the FEG-SEM imagens, with the presence of Co-NC-Fe catalyst not only at the top of the film but also inside and between the α-Fe_2O_3 nanorods. This suggests that the α-Fe_2O_3 nanorods are in close contact with Co-NC-Fe particles at the boundaries. Hence, the generated electrons can be captured by the Co^{II}-NC-Fe^{III} particles inside the film, reducing Fe^{III} to Fe^{II}. Meanwhile, Fe^{III} regeneration may be achieved by the application of an external bias, as observed in the increase of the 2190 cm^{-1} signal under light illumination (E = 1.0 V, Figure 6d), suggesting the presence of a backward reaction that forms $[Fe(CN)_6]^{3-}$.

In contrast, *in situ* FTIR spectra did not show significant evidence of Fe^{II} oxidation in Co^{II}-NC-Fe^{II} as well as α-Fe_2O_3/Co^{II}-NC-Fe^{II}. Additional evidence for the resistance toward the oxidation of Fe^{II} to Fe^{III} in Co^{II}-NC-Fe^{II} is the CV curves in Figure S12, where a smaller capacitive current was observed for the α-Fe_2O_3/Co^{II}-NC-Fe^{II} photoanode, compared to the other Co-NC-Fe material. These facts will probably affect the charge carrier recombination rate since electrons from the CB of α-Fe_2O_3 cannot be transferred to Fe^{III} species and reduce them. Consequently, the electron/hole recombination reaction overwhelms water oxidation. The greater photocurrent density for α-Fe_2O_3/Co^{II}-NC-Fe^{II} compared to the bare α-Fe_2O_3 photoanode is probably influenced by the modification of surface states that make charge transfer kinetically favorable.[54]

Apart from the intrinsic property of the materials, the synergistic effect, and the energy level modification of the surface states in the α-Fe_2O_3 photoanodes suggested by recent works,[31,54] we have shown, based on our recent outcomes by *in situ* characterization that the PEC performance of the α-Fe_2O_3/Co-NC-Fe photoanodes is also dependent on the difference in the oxidation states of the elements in the Co-NC-Fe structure analogues in their starting materials. In addition, the whole process demands thermodynamic and kinetic properties, and the efficiency of the PEC performance is fundamentally governed by the morphology, defect sites, photoactive area of the electrode, and stoichiometric ratio, which in fact affect the capability of the surface to avoid electron trapping or recombination by photogenerated holes.[68]

In this work, the incorporation of Co-NC-Fe has proven to greatly impact such properties toward the achievement of better PEC performance. *In situ* FTIR shows the oxidation of Co^{II} to Co^{III} in both photoanodes; however, solar light enhances the generation of reversible Fe^{II}/Fe^{III} redox pairs, supporting the process proposed in Figure 7, which could be the main cause for the electron/hole pair lifetime enhancement measured by TAS. Due to intrinsic drawbacks of α-Fe_2O_3 that hamper its use as an effective photoanode, Co-NC-Fe incorporation showed a promising potential for other semiconductors and for the development of electrocatalysts for PEC water splitting, especially under mild and neutral conditions.

4. CONCLUSIONS

In the present work, we described the improvement of the photocurrent density of α-Fe_2O_3/Co-NC-Fe photoanodes compared to bare α-Fe_2O_3. Given the complexity of chemical changes that take place in α-Fe_2O_3/Co-NC-Fe photoanodes, we showed the fundamental understanding of different mechanisms with the contribution of *in situ* techniques for materials characterization. Despite both Co-NC-Fe materials leading to a higher PEC performance, Co^{II}-NC-Fe^{III} showed stronger influence on photocurrent generation. In summary, owing to the synergistic effect between α-Fe_2O_3 and Co-NC-Fe particles, the resulting α-Fe_2O_3/Co^{II}-NC-Fe^{III} photoanode exhibited a better PEC performance compared to the α-Fe_2O_3/Co^{II}-NC-Fe^{II} photoanode. The difference between their PEC performances was understood by the generation of reversible Fe^{II}/Fe^{III} redox pairs in the α-Fe_2O_3/Co^{II}-NC-Fe^{III} photoanode, which mitigates charge carrier recombination, thereby

https://dx.doi.org/10.1021/acsaem.0c01782
ACS Appl. Energy Mater. 2020, 3, 10097−10107

allowing holes available to drive water oxidation. α-Fe_2O_3/Co^{II}-NC-Fe^{II} was found to not oxidize Fe^{II} to Fe^{III}, so charge recombination predominates, leading to a lower PEC performance. In this work, we showed the vital importance of understanding the mechanisms underlying charge separation and transport for materials development of better photoanodes. Further efforts must be made to synthesize stable (α-Fe_2O_3/Co-NC-Fe)-based materials as a viable approach with appropriate band-edge alignments for oxygen evolution experiments without the need of an applied bias and/or under mild conditions.

■ ASSOCIATED CONTENT

Supporting Information

The Supporting Information is available free of charge at https://pubs.acs.org/doi/10.1021/acsaem.0c01782.

The EDX of the cross-sectional images of the films; CV measurements of α-Fe_2O_3/Co-NC-Fe photoanodes; XPS spectra of photoanodes; and full FTIR spectra of photoanodes (PDF)

■ AUTHOR INFORMATION

Corresponding Authors

Ana Flávia Nogueira − *Institute of Chemistry, University of Campinas (UNICAMP), Campinas, São Paulo 13083-970, Brazil;* orcid.org/0000-0002-0838-7962; Email: anafla@unicamp.br

Juliano Alves Bonacin − *Institute of Chemistry, University of Campinas (UNICAMP), Campinas, São Paulo 13083-970, Brazil;* orcid.org/0000-0001-9399-1031; Email: jbonacin@unicamp.br

Authors

Saulo Amaral Carminati − *Institute of Chemistry, University of Campinas (UNICAMP), Campinas, São Paulo 13083-970, Brazil;* orcid.org/0000-0001-8429-8788

Bruno Leuzinger da Silva − *Institute of Chemistry, University of Campinas (UNICAMP), Campinas, São Paulo 13083-970, Brazil*

José Luiz Bott-Neto − *Institute of Chemistry, University of Campinas (UNICAMP), Campinas, São Paulo 13083-970, Brazil;* orcid.org/0000-0003-1806-3280

Mauricio Alves de Melo, Jr. − *Institute of Physics, University of São Paulo (USP), São Carlos, São Paulo 13560-970, Brazil;* orcid.org/0000-0001-7276-3179

Miguel Tayar Galante − *Institute of Chemistry, University of Campinas (UNICAMP), Campinas, São Paulo 13083-970, Brazil*

Pablo Sebástian Fernández − *Institute of Chemistry, University of Campinas (UNICAMP), Campinas, São Paulo 13083-970, Brazil;* orcid.org/0000-0002-5068-0556

Claudia Longo − *Institute of Chemistry, University of Campinas (UNICAMP), Campinas, São Paulo 13083-970, Brazil;* orcid.org/0000-0001-8955-148X

Complete contact information is available at: https://pubs.acs.org/10.1021/acsaem.0c01782

Funding

This work was supported by the Brazilian agency FAPESP (Grant Nos. 2015/23775-3, 2017/11986-5, 2018/20952-0, and 2017/23960-0), CNPq, and Shell. This study was also financed in part by the Coordenação de Aperfeiçoamento de Pessoal de Nível Superior - Brasil (CAPES), Finance Code 001, and by ANP (Brazil's National Oil, Natural Gas and Biofuels Agency) through the research and development levy regulation.

Notes

The authors declare no competing financial interest.

■ ACKNOWLEDGMENTS

The authors gratefully acknowledge Renato Vitalino Gonçalves from USP-São Carlos for providing access to XPS measurements.

■ REFERENCES

(1) Liu, J.; Liu, Y.; Liu, N.; Han, Y.; Zhang, X.; Huang, H.; Lifshitz, Y.; Lee, S. − T.; Zhong, J.; Kang, Z. Metal free efficient photocatalyst for stable visible water splitting via a two-electron pathway. *Science* **2015**, *347* (6225), 970−974.

(2) Lhermitte, C. R.; Garret Verwer, J.; Bartlett, B. M. Improving the stability and selectivity for the oxygen evolution reaction on semiconducting WO_3 photoelectrodes with a solid-state FeOOH catalyst. *J. Mater. Chem. A* **2016**, *4*, 2960−2968.

(3) Li, P.; Zhao, R.; Chen, H.; Wang, H.; Wei, P.; Huang, H.; Liu, Q.; Li, T.; Shi, X.; Zhang, Y.; Liu, M.; Sun, X. Recent Advances in the Development of Water Oxidation Electrocatalysts at Mild pH. *Small* **2019**, *15*, 1805103.

(4) Kim, J. Y.; Magesh, G.; Youn, D. H.; Jang, J. − W.; Kubota, J.; Domen, K.; Lee, J. S. Single-crystalline, wormlike hematite photoanodes for efficient solar water splitting. *Sci. Rep.* **2013**, *3*, 2681.

(5) Dias, P.; Andrade, L.; Mendes, A. Hematite-based photoelectrode for water splitting with very high photovoltage. *Nano Energy* **2017**, *38*, 218−231.

(6) Gurudayal; Bassi, P. S.; Sritharan, T.; Wong, L. H. Recent Progress in iron oxide based photoanodes for solar water splitting. *J. Phys. D: Appl. Phys.* **2018**, *51*, 473002.

(7) Annamalai, A.; Subramanian, A.; Kang, U.; Park, H.; Choi, S. H.; Jang, J. S. Activation of Hematite Photoanodes for Solar Water Splitting: Effect of FTO Deformation. *J. Phys. Chem. C* **2015**, *119*, 3810−3817.

(8) Tamirat, A. G.; Rick, J.; Dubale, A. A.; Su, W. − N.; Hwang, B. − J. Using hematite for photoelectrochemical water splitting: a review of current progress and challenges. *Nanoscale Horiz.* **2016**, *1*, 243−267.

(9) Ho-Kimura, S.; Williamson, B. A. D.; Sathasivam, S.; Moniz, S. J. A.; He, G.; Luo, W.; Scanlon, D. O.; Tang, J.; Parkin, I. P. Origin of High-Efficiency Photoelectrochemical Water Splitting on Hematite/Functional Nanohybrid Metal Oxide Overlayer Photoanode after a Low Temperature Iner Gas Annealing Treatment. *ACS Omega.* **2019**, *4* (1), 1449−1459.

(10) Tang, P.; Arbiol, J. Engineering surface states of hematite based photoanodes for boosting photoelectrochemical water splitting. *Nanoscale Horiz.* **2019**, *4*, 1256−1276.

(11) Schrantz, K.; Wyss, P. P.; Ihssen, J.; Toth, R.; Bora, D. K.; Vitol, E. A.; Rozhkova, E. A.; Pieles, U.; Thony-Meyer, L.; Braun, A. Hematite photoanode co-functionalized with self-assembling melanin and C-phycocyanin for solar water splitting at neutral pH. *Catal. Today* **2017**, *284*, 44−51.

(12) Shen, S. Toward efficient solar water splitting over hematite photoelectrodes. *J. Mater. Res.* **2014**, *29*, 29−36.

(13) Malviya, K. D.; Dotan, H.; Shlenkevich, D.; Tsyganok, A.; Mor, H.; Rothschild, A. Systematic comparision of different dopants in thind film hematite (α-Fe_2O_3) photoanodes for solar water splitting. *J. Mater. Chem. A* **2016**, *4*, 3091−3099.

(14) Ling, Y.; Wang, G.; Wheeler, D. A.; Zhang, J. Z.; Li, Y. Sn-Doped Hematite Nanostructures for photoelectrochemical Water Splitting. *Nano Lett.* **2011**, *11*, 2119−2125.

(15) Li, S.; Cai, J.; Liu, Y.; Gao, M.; Cao, F.; Qin, G. Tuning orientation of doped hematite photoanodes for enhanced photo-

electrochemical water oxidation. *Sol. Energy Mater. Sol. Cells* **2018**, *179*, 328−333.
(16) Yan, K.; Qiu, Y.; Xiao, S.; Gong, J.; Zhao, S.; Xu, J.; Meng, X.; Yang, S.; Xu, J. Self-driven hematite based photoelectrochemical water splitting cells with three-dimensional nanobowl heterojunction and high-photovoltage perovskite solar cells. *Mater. Today Energy.* **2017**, *6*, 128−135.
(17) Shen, S.; Lindley, S. A.; Chen, X.; Zhang, J. Z. Hematite heterostructures for photoelectrochemical water splitting: rational materials design and charge carrier dynamics. *Energy Environ. Sci.* **2016**, *9*, 2744−2775.
(18) Wang, L.; Nguyen, N. T.; Schmuki, P. A Facile Surface Passivation of Hematite Photoanodes with Iron, Titanate Cocatalyst for Enhanced Water Splitting. *ChemSusChem* **2016**, *9*, 2048−2053.
(19) Shen, S.; Li, M.; Guo, L.; Jiang, J.; Mao, S. S. Surface passivation of undoped hematite nanorod arrays via aqueous solution growth for improved photoelectrochemical water splitting. *J. Colloid Interface Sci.* **2014**, *427*, 20−24.
(20) Barroso, M.; Mesa, C. A.; Pendlebury, S. R.; Cowan, A. J.; Hisatomi, T.; Sivula, K.; Grätzel, M.; Klug, D. R.; Durrant, J. R. Dynamics of photogenerated holes in surface modified α-Fe_2O_3 photoanodes for solar water splitting. *Proc. Natl. Acad. Sci. U. S. A.* **2012**, *109*, 15640−15645.
(21) Bonhommeau, S.; Pontius, N.; Cobo, S.; Salmon, L.; de Groot, F. M. F.; Molnar, G.; Bousseksou, A.; Durr, H. A.; Eberhardt, W. Metal-to-ligand and ligand-to-metal charge transfer in thin films of Prussian blue analogues investigated by X-ray abosorption spectroscopy. *Phys. Chem. Chem. Phys.* **2008**, *10*, 5882−5889.
(22) Zhao, F.; Wang, Y.; Xu, X.; Liu, Y.; Song, R.; Lu, G.; Li, Y. Cobalt Hexacyanoferrate Nanoparticles as a High-Rate and Ultrastable Supercapacitor Electrode Material. *ACS Appl. Mater. Interfaces* **2014**, *6*, 11007−11012.
(23) Qin, Z.; Li, Y.; Gu, N. Progress in Applications of Prussian blue Nanoparticles in Biomedicine. *Adv. Healthcare Mater.* **2018**, *7*, 1800347.
(24) Aller-Pellitero, M.; Fremeau, J.; Villa, R.; Guirado, G.; Lakard, B.; Hihn, J. − Y.; del Campo, F. J. Electrochromic biosensors based on screen-printed Prussian Blue electrodes. *Sens. Actuators, B* **2019**, *290*, 591−597.
(25) Lee, S. H.; Chung, J.-H.; Park, H.-K.; Lee, G.-J. A Simple and Facile Glucose Biosensor Based on Prussian Blue Modified Graphite String. *J. Sens.* **2016**, *2016*, 1859292.
(26) Karyakin, A. A. Advances of Prussian blue and its analogues in (bio)sensors. *Curr. Opin. Electrochem.* **2017**, *5*, 92−98.
(27) Pires, B. M.; dos Santos, P. L.; Katic, V.; Strohauer, S.; Landers, R.; Formiga, A. L. B.; Bonacin, J. A. Electrochemical water oxidation by cobalt-Prussian blue coordination polymer and theoretical studies of the electronic structure of active species. *Dalton Trans.* **2019**, *48*, 4811−4822.
(28) Alsac, E. P.; Ulker, E.; Nune, S. V. K.; Dede, Y.; Karadas, F. Tuning the Electronic Properties of Prussian Blue Analogues for Efficient Water Oxidation Electrocatalysis: Experimental and Computational Studies. *Chem. - Eur. J.* **2018**, *24*, 4856−4863.
(29) Pintado, S.; Goberna-Ferrón, S.; Escudero-Adán, E. C.; Galán-Mascarós, J. R. Fast and persistent electrocatalytic water oxidation by Co-Fe prussian blue coordination polymers. *J. Am. Chem. Soc.* **2013**, *135*, 13270−13273.
(30) Rodriguez-Garcia, B.; Reyes-Carmona, A.; Jimenez-Morales, I.; Blasco-Ahicart, M.; Cavaliere, S.; Dupont, M.; Jones, D.; Roziere, J.; Galan-Mascaros, J. R.; Jaouen, F. Cobalt hexacyanoferrate supported on Sb-doped SnO_2 as a non-noble catalyst for oxygen evolution in acidic medium. *Sustainable Energy Fuels.* **2018**, *2*, 589−597.
(31) Hegner, F. S.; Cardenas-Morcoso, D.; Giménez, S.; López, N.; Galan-Máscaros, J. R. Level Alignment as Descriptor for Semiconductor/Catalyst Systems In Water Splitting: The Case of Hematite/Cobalt Hexacyanoferrate Photoanodes. *ChemSusChem* **2017**, *10*, 4552−4560.
(32) Amaral Carminati, S.; do Nascimento Barbosa, A.; Luiz Martins de Freitas, A.; Freire, F. L.; Souza, F. L.; Nogueira, A. F. Unraveling the role of single layer graphene as overlayer on hematite photoanodes. *J. Catal.* **2019**, *372*, 109−118.
(33) Cui, W.; Niu, W.; Wick-Joliat, R.; Moehl, T.; Tilley, S. D. Operando deconvolution of photovoltaic and electrocatalytic performance in ALD TiO_2 protected water splitting photocathodes. *Chem. Sci.* **2018**, *9*, 6062−6067.
(34) Yuan, Y.; Li, M.; Bai, Z.; Jiang, G.; Liu, B.; Wu, T.; Chen, Z.; Amine, K.; Lu, J. The Absence and Importance of Operando Techniques for Metal-Free Catalysts. *Adv. Mater.* **2019**, *31*, 1805609.
(35) Li, X.; Yang, X.; Zhang, J.; Huang, Y.; Liu, B. In situ/Operando Techniques for Characterization of Single-Atom Catalysts. *ACS Catal.* **2019**, *9* (3), 2521−2531.
(36) Cen, J.; Wu, Q.; Liu, M.; Orlov, A. Developing new understanding of photoelectrochemical water splitting via in-situ techniques: A review on recent progress. *Green Energy Environ.* **2017**, *2*, 100−111.
(37) Liang, Z.; Zou, Q.; Wang, Yu.; Lu, Y. − C. Recent Progress in Applying In Situ/Operando Characterization Techniques to Probe the Solid/Liquid/Gas Interfaces of Li-O_2 Batteries. *Small Methods.* **2017**, *1*, 1700150.
(38) Sarker, S.; Lamb, J. J.; Hjelme, D. R.; Lien, K. M. Overview of recent progress towards in-situ biogas upgradation techniques. *Fuel* **2018**, *226*, 686−697.
(39) Nakamura, R.; Imanishi, A.; Murakoshi, K.; Nakato, Y. In situ FTIR Studies of Primary Intermediates of Photocatalytic Reactions on Nanocrystalline TiO_2 Films in Contact with Aqueous Solutions. *J. Am. Chem. Soc.* **2003**, *125*, 7443−7450.
(40) Murcia, J.; Hidalgo, M. C.; Navío, J. A.; Araña, J.; Dõna-Rodríguez, J. M. In situ FT-IR study of the adsorption and photocatalytic oxidation of ethanol over sulfated and metallized TiO_2. *Appl. Catal., B* **2013**, *142*, 205−213.
(41) Wu, J. C. S.; Cheng, Y. − T. In Situ FTIR study of photocatalytic NO reaction on photocatalysts under UV irradiation. *J. Catal.* **2006**, *237*, 393−404.
(42) Iwasita, T.; Nart, F. C. In situ infrared spectroscopy at electrochemical interfaces. *Prog. Surf. Sci.* **1997**, *55*, 271−340.
(43) Bott-Neto, J. L.; Rodrigues, M. V. F.; Silva, M. C.; Carneiro-Neto, E. B.; Wosiak, G.; Mauricio, J. C.; Pereira, E. C.; Figueroa, S. J. A.; Fernandez, P. S. Versatile Spectroelectrochemical Cell for In Situ Experiments: Development, Applications, and Electrochemical Behavior. *ChemElectroChem* **2020**, *7*, 1−9.
(44) Li, P.; Jiang, E. Y.; Bai, H. L. Fabrication of ultrathin epitaxial μ-Fe_2O_3 films by reactive sputtering. *J. Phys. D: Appl. Phys.* **2011**, *44*, No. 075003.
(45) Cai, W.-R.; Zhang, G.-Y.; Song, T.; Zhang, X.-J.; Shan, D. Cobalt hexacyanoferrate electrodeposited on electrode with assistance of laponite: The enhanced electrochemical sensing of captoril. *Electrochim. Acta* **2016**, *198*, 32−39.
(46) Yamada, M.; Arai, M.; Kurihara, M.; Sakamoto, M.; Miyake, M. Synthesis and Isolation of Cobalt Hexacyanoferrate/Chromate Metal Coordination Nanopolymers Stabilized by Alkylamino Ligand with Metal Elemental Control. *J. Am. Chem. Soc.* **2004**, *126*, 9482−9483.
(47) Li-Hong, S.; Tian, W.; Mei-Jia, W.; Di, L.; Yuan-Jian, Z.; Jing-Hong, L. Molecule-Based Cobalt Hexacyanoferrate Nanoparticle: Synthesis, Characterization and Its Electrochemical Properties. *Chin. J. Chem.* **2005**, *23*, 149−154.
(48) Gray, H. B.; Beach, N. A. The Electronic Structures of Octahedral Metal Complexes. I. Metal Hexacarbonyls and Hexacyanides. *J. Am. Chem. Soc.* **1963**, *85*, 2922−2927.
(49) Kholoud, E.; Watanabe, H.; Takahashi, A.; Emara, M. M.; Abd-El-Nabey, B. A.; Kurihara, M.; Tajima, K.; Kawamoto, T. Cobalt hexacyanoferrate nanoparticles for wet-processed brown-bleached electrochromic devices with hybridization of high-spin/low-spin phases. *J. Mater. Chem. C* **2017**, *5*, 8921.
(50) Sato, O.; Einaga, Y.; Fujishima, A.; Hashimoto, K. Photoinduced Long-Range Magnetic Ordering of Cobalt-Iron Cyanide. *Inorg. Chem.* **1999**, *38*, 4405−4412.
(51) Zambiazi, P.; de Moraes, A.; Kogachi, R.; Aparecido, G.; Formiga, A.; Bonacin, J. Performance of water oxidation by 3D

https://dx.doi.org/10.1021/acsaem.0c01782
ACS Appl. Energy Mater. 2020, 3, 10097−10107

printed electrodes modified by prussian blue analogues. *J. Braz. Chem. Soc.* **2020**, *0*, 1−12.
(52) Kim, J. Y.; Jang, J.-W.; Youn, D. H.; Magesh, G.; Lee, J. S. A Stable and Efficient Hematite Photoanode in a Neutral Electrolyte for Solar Water Splitting: Towards Stability Engineering. *Adv.Energy Mater.* **2014**, *4*, 1400476.
(53) Yang, Y.; Brownell, C.; Sadrieh, N.; May, J.; del Grosso, A.; Place, D.; Leutzinger, E.; Duffy, E.; He, R.; Houn, F.; Lyon, R.; Faustino, P. Quantitative measurement of cyanide released from Prussian Blue. *Clin. Toxicol.* **2007**, *45*, 776.
(54) Tang, P. − Y.; Han, L.-J.; Hegner, F. S.; Paciok, P.; Biset-Peiró, M.; Du, H.-C.; Wei, X.-K.; Jin, L.; Xie, H.-B.; Shi, Q.; Andreu, T.; Lira-Cantú, M.; Heggen, M.; Dunin-Borkowski, R. E.; López, N.; Galán-Mascarós, J. R.; Morante, J. R.; Arbiol, J. Boosting Photoelectrochemical Water Oxidation of Hematite in Acidic Electrolytes by Surface State Modification. *Adv. Energy Mater.* **2019**, *9*, 1901836.
(55) Gurudayal; Chiam, S. Y.; Kumar, M. H.; Bassi, P. S.; Seng, H. L.; Barber, J.; Wong, L. H. *ACS Appl. Mater. Interfaces* **2014**, *6*, 5852−5859.
(56) Wang, T.; Zhou, S.; Zhang, C.; Lian, C.; Liang, Y.; Yuan, W. Facile synthesis of hematite nanoparticles and nanocubes and their shape-dependent optical properties. *New J. Chem.* **2014**, *38*, 46−49.
(57) Pendlebury, S. R.; Wang, X.; Le Formal, F.; Cornuz, M.; Kafizas, A.; Tilley, S. D.; Grätzel, M.; Durrant, J. R. Ultrafast Charge Carrier Recombination and Trapping in Hematite Photoanodes under Applied Bias. *J. Am. Chem. Soc.* **2014**, *136*, 9854−9857.
(58) Pei, G. X.; Wijten, J. H. J.; Weckhuysen, B. M. Probing the dynamics of photogenerated holes in doped hematite photoanodes for solar water splitting using transient absorption spectroscopy. *Phys. Chem. Chem. Phys.* **2018**, *20*, 9806.
(59) Kulesza, P. J.; Malik, M. A.; Denca, A.; Strojek, J. In Situ FT-IR/ATR Spectroelectrochemistry of Prussian Blue in the Solid State. *Anal. Chem.* **1996**, *68*, 2442−2446.
(60) Lezna, R. O.; Romagnoli, R.; de Tacconi, N. R.; Rajeshwar, K. Cobalt Hexacyanoferrate: Coumpound Stoichiometry, Infrared Spectroelectrochemistry, and Photoinduced Electron Transfer. *J. Phys. Chem. B* **2002**, *106*, 3612−3621.
(61) Moss, B.; Hegner, F. S.; Corby, S.; Selim, S.; Francas, L.; Lopez, N.; Gimenez, S.; Galan-Mascaros, J.-R.; Durrant, J. R. Unraveling Charge Transfer in CoFe Prussian Blue Modified $BiVO_4$ Photoanodes. *ACS Energy Lett.* **2019**, *4*, 337−342.
(62) Nart, F. C.; Iwasita, T. In Situ FTIR as a Tool for Mechanistic Studies. Fundamentals and Applications. In *Encyclopedia of Electrochemistry: Online*; Wiley-VCH Verlag GmbH & Co., 2007.
(63) Berrettoni, M.; Giorgetti, M.; Zamponi, S.; Conti, P.; Ranganathan, D.; Zanotto, A.; Saladino, M. L.; Caponetti, E. Synthesis and Characterization of Nanostructured Cobalt Hexacyanoferrate. *J. Phys. Chem. C* **2010**, *114*, 6401−6407.
(64) Bordage, A.; Moulin, R.; Fonda, E.; Fornasieri, G.; Rivière, E.; Bleuzen, A. Evidence of the core-shell structure of (photo)magnetic CoFe prussian blue analogue nanoparticles peculiar behavior of the surface species. *J. Am. Chem. Soc.* **2018**, *140*, 10332−10343.
(65) Miseki, Y.; Sayama, K. Photocatalytic water splitting employing a $[Fe(CN)_6]^{3-/4-}$ redox mediatior under visible light. *Catal. Sci. Technol.* **2019**, *9*, 2019−2024.
(66) Yamamoto, T.; Saso, N.; Umemura, Y.; Einaga, Y. Photoreduction of Prussian Blue into Titania Nanosheet Ultrathin Films. *J. Am. Chem. Soc.* **2009**, *131*, 13196−13197.
(67) Baumanis, C.; Bloh, J. Z.; Dillert, R.; Bahnemann, D. W. Hematite Photocatalysis: Dechlorination of 2,6-Dichloroindophenol and Oxidation of Water. *J. Phys. Chem. C* **2011**, *115*, 25442−25450.
(68) Bedin, K. C.; Muche, D. N. F.; Melo, M. A.; Freitas, A. L. M.; Goncalves, R. V.; Souza, F. L. Role of cocatalysts on hematite photoanodes in photoelectrocatalytic water splitting: challegenes and future perspectives. *ChemCatChem* **2020**, *12*, 3156−3169.

https://dx.doi.org/10.1021/acsaem.0c01782
ACS Appl. Energy Mater. 2020, 3, 10097−10107